



**AFRL-RX-WP-TP-2012-0350**

**A COMPREHENSIVE STRUCTURAL ANALYSIS  
PROCESS FOR FAILURE ASSESSMENT IN AIRCRAFT  
LAP-JOINT MIMICS USING MULTI-MODAL FUSION OF  
NDE DATA (PREPRINT)**

**Soumya De, R. Joe Stanley, Mohammad T. Ghasr, Reza Zoughi, Kenneth Doering, David Van Aken, and Matt O'Keefe**

**Missouri University of Science and Technology**

**Kapil Gupta  
Coherix, Inc.**

**Donald Palmer  
The Boeing Company**

**Gary Steffes  
Metals Branch  
Structural Materials Division**

**JULY 2012  
Final Report**

**Approved for public release; distribution unlimited.**

*See additional restrictions described on inside pages*

**STINFO COPY**

**AIR FORCE RESEARCH LABORATORY  
MATERIALS AND MANUFACTURING DIRECTORATE  
WRIGHT-PATTERSON AIR FORCE BASE, OH 45433-7750  
AIR FORCE MATERIEL COMMAND  
UNITED STATES AIR FORCE**

REPORT DOCUMENTATION PAGE					Form Approved OMB No. 0704-0188	
<p>The public reporting burden for this collection of information is estimated to average 1 hour per response, including the time for reviewing instructions, searching existing data sources, gathering and maintaining the data needed, and completing and reviewing the collection of information. Send comments regarding this burden estimate or any other aspect of this collection of information, including suggestions for reducing this burden, to Department of Defense, Washington Headquarters Services, Directorate for Information Operations and Reports (0704-0188), 1215 Jefferson Davis Highway, Suite 1204, Arlington, VA 22202-4302. Respondents should be aware that notwithstanding any other provision of law, no person shall be subject to any penalty for failing to comply with a collection of information if it does not display a currently valid OMB control number. <b>PLEASE DO NOT RETURN YOUR FORM TO THE ABOVE ADDRESS.</b></p>						
1. REPORT DATE (DD-MM-YY) July 2012		2. REPORT TYPE Technical Paper		3. DATES COVERED (From - To) 1 June 2012 – 1 July 2012		
4. TITLE AND SUBTITLE A COMPREHENSIVE STRUCTURAL ANALYSIS PROCESS FOR FAILURE ASSESSMENT IN AIRCRAFT LAP-JOINT MIMICS USING MULTI-MODAL FUSION OF NDE DATA (PREPRINT)				5a. CONTRACT NUMBER FA8650-04-C-5704		
				5b. GRANT NUMBER		
				5c. PROGRAM ELEMENT NUMBER 62102F		
6. AUTHOR(S) Soumya De, R. Joe Stanley, Mohammad T. Ghasr, Reza Zoughi, Kenneth Doering, David Van Aken, and Matt O'Keefe (Missouri University of Science and Technology) Kapil Gupta (Coherix, Inc.) Donald Palmer (The Boeing Company) Gary Steffes (AFRL/RXCM)				5d. PROJECT NUMBER 4347		
				5e. TASK NUMBER 00		
				5f. WORK UNIT NUMBER 25100000		
7. PERFORMING ORGANIZATION NAME(S) AND ADDRESS(ES) Missouri University of Science and Technology 300 West 12 Street Rolla, MO 65409				8. PERFORMING ORGANIZATION REPORT NUMBER AFRL-RX-WP-TP-2012-0350		
9. SPONSORING/MONITORING AGENCY NAME(S) AND ADDRESS(ES) Air Force Research Laboratory Materials and Manufacturing Directorate Wright-Patterson Air Force Base, OH 45433-7750 Air Force Materiel Command United States Air Force				10. SPONSORING/MONITORING AGENCY ACRONYM(S) AFRL/RXCM		
				11. SPONSORING/MONITORING AGENCY REPORT NUMBER(S) AFRL-RX-WP-TP-2012-0350		
12. DISTRIBUTION/AVAILABILITY STATEMENT Approved for public release; distribution unlimited. Preprint to be submitted to IEEE Transactions on Instrumentation and measurement						
13. SUPPLEMENTARY NOTES The U.S. Government is joint author of this work and has the right to use, modify, reproduce, release, perform, display, or disclose the work. PA Case Number and clearance date: 88ABW-2012-3696, 26 June 2012. This document contains color.						
14. ABSTRACT Multi-modal data fusion techniques are commonly used to enhance decision-making processes. In previous research, a comprehensive structural analysis process was developed for quantizing and evaluating characteristics of defects in aircraft lap-joint mimics using eddy current nondestructive evaluation (NDE) data collected for structural health monitoring. In this research, a comprehensive multi-modal structural analysis process is presented that includes intra- and inter-modal NDE data fusion. The process includes defect detection, defect characterization and Finite Element Modeling-based simulated fatigue testing for structural analysis. The multi-modal structural analysis process is then experimentally evaluated using five lap-joint mimic test panels with corroded patches at different layers of the lap-joints and one painted pristine panel used as a reference. The test panels are subjected to two rounds of mechanical loading, preceded by eddy current, millimeter wave, and ultrasonic NDE data obtained prior to each round. Different modality combinations are used to model the test panels at the different rounds of measurements.						
15. SUBJECT TERMS multi-modal data fusion, nondestructive evaluation, structural health monitoring						
16. SECURITY CLASSIFICATION OF:			17. LIMITATION OF ABSTRACT: SAR	NUMBER OF PAGES 36	19a. NAME OF RESPONSIBLE PERSON (Monitor) Todd J. Turner 19b. TELEPHONE NUMBER (Include Area Code) N/A	
a. REPORT Unclassified	b. ABSTRACT Unclassified	c. THIS PAGE Unclassified				

# **A COMPREHENSIVE STRUCTURAL ANALYSIS PROCESS FOR FAILURE ASSESSMENT IN AIRCRAFT LAP-JOINT MIMICS USING MULTI-MODAL FUSION OF NDE DATA**

Soumya De<sup>a</sup>, Kapil Gupta<sup>b</sup>, R. Joe Stanley<sup>a</sup>, Mohammad T. Ghasr<sup>a</sup>, Reza Zoughi<sup>a</sup>, Kenneth Doering<sup>c</sup>, David Van Aken<sup>c</sup>, Gary Steffes<sup>d</sup>, Matt O'Keefe<sup>c</sup>, Donald Palmer<sup>e</sup>

<sup>a</sup> Department of Electrical and Computer Engineering, Missouri University of Science and Technology (S&T), Rolla, MO, 65409, USA

<sup>b</sup> Coherix Inc., Ann Arbor, MI, 66062, USA

<sup>c</sup> Department of Materials Science & Engineering, Missouri University of Science and Technology (S&T), Rolla, MO, 65409, USA

<sup>d</sup> Air Force Research Laboratory (AFRL), Wright Patterson, OH 45433, USA

<sup>e</sup> The Boeing Company, Boeing Phantom Works, St. Louis, MO 63166, USA

## **ABSTRACT:**

Multi-modal data fusion techniques are commonly used to enhance decision-making processes. In previous research, a comprehensive structural analysis process was developed for quantizing and evaluating characteristics of defects in aircraft lap-joint mimics using eddy current nondestructive evaluation (NDE) data collected for structural health monitoring. In this research, a comprehensive multi-modal structural analysis process is presented that includes intra- and inter-modal NDE data fusion. The process includes defect detection, defect characterization and Finite Element Modeling-based simulated fatigue testing for structural analysis. The multi-modal structural analysis process is then experimentally evaluated using five lap-joint mimic test panels with corroded patches at different layers of the lap-joints and one painted pristine panel used as a reference. The test panels are subjected to two rounds of mechanical loading, preceded by eddy current, millimeter wave, and ultrasonic NDE data obtained prior to each round. Different modality combinations are used to model the test panels at the different rounds of measurements. Experiments are performed to compare the simulated fatigue loading based on models determined from different modality combinations and the mechanical loading results to find susceptible-to-failure areas in the test panels. The results show that the comprehensive structural analysis process found the correct locations of failure areas at rates as high as 98.8%, using eddy current and ultrasonic modalities.

*Index terms: Multi-Modal Data Fusion, Nondestructive Evaluation, Structural Health Monitoring.*

## **I. INTRODUCTION:**

Corrosion-induced aircraft structural degradation is the subject of constant attention and concern for those involved in maintaining operational integrity and safety of aging aircraft fleets (i.e., commercial, cargo and military). Hidden corrosion under paint or in between various lap-joint layers tends to facilitate early fatigue crack initiation and enhanced crack growth when the aircraft experiences in-service loadings [1, 2]. To this end, the U.S. Air Force has proposed a “predict and manage” scheme for corrosion management as a deviation from the current “find-it and fix-it” approach [3].

To characterize and evaluate corrosion in aging aircraft structures many nondestructive evaluation (NDE) methods have been explored in the past and are currently being implemented [4-11]. In general, NDE methods may provide qualitative information (e.g., corroded or not) and/or quantitative evaluation (e.g., corrosion thickness/severity, spatial extent, etc.) about a structure. Also, each NDE method used for corrosion detection has its own limitations and advantageous features as outlined in detail in [8]. Some of the more prominent methods for aircraft structural integrity analysis, and more specifically for corrosion evaluation, include eddy current (EC), ultrasonic (UT), optical, thermography, radiography and millimeter wave (MW) methods [8].

EC inspection systems are small, portable and inexpensive, and are capable of providing effective metal loss information. Both pulsed and conventional EC NDE methods have been used for corrosion detection in aging aircrafts [5-7]. Conventional EC methods can be used to provide structural metal loss/thinning information, while pulsed EC methods provide material loss depth information as well[10].

Ultrasonic methods are effective inspection tools for a number of NDE applications and employ high frequency sound waves (with relatively short wavelengths in the material).

Ultrasonic signal amplitude, frequency or time of flight (ToF) may be used to detect and evaluate a number of defect characteristics. UT can be limited in its capability to distinguish features in subsequent structural layers underneath the surface layer. This is due to the lack of an effective UT coupling media between layers. In contrast, EC is not limited by these constraints, has a relatively high signal to noise ratio, and is able to provide depth information as well [4, 10].

Millimeter wave NDE methods offer several important advantages for detection and evaluation of corrosion under paint and thick composite laminate coatings [9, 12, 13]. Millimeter wave signals can penetrate inside of low-loss dielectric materials and interact with their inner structure. They are also sensitive to changes associated with dielectric properties and boundary interfaces, which make them very attractive for detecting the presence of undesired layers such as corrosion under paint. Near-field MW NDE techniques, employing open-ended rectangular waveguide probes, have been successfully used to detect the presence of corrosion and corrosion precursor pitting under paint and primer in both steel and aluminum substrates [9, 12-17]. However, MW signals do not penetrate inside of electrically conducting materials such as metals and can therefore only provide information about surface flaws such as pitting and corrosion under paint or dielectric coatings. Therefore, as it relates to the objectives of this investigation and when considering a lap joint made of several aluminum panels, other methods must be employed to detect corrosion in between the various layers of the lap joints.

Results of previous research have clearly demonstrated that an effective way to overcome the limitations of each NDE method is to integrate several of these NDE data using multi-modal data fusion techniques. In this way the complementary information across the various NDE

modalities can be effectively combined to provide significantly more information than any one method can, resulting in substantial increase in measurement reliability. Using complementary information, data fusion techniques have the potential to provide a much better and more comprehensive understanding of the physical process, which in this case is corrosion, as compared to using one sensor data or using multiple sensors in an independent manner [4, 8, 10, 18]. Data fusion provides a mathematical framework to enhance the data analysis process based on data collected from a single modality and processed using multiple methods (intra-modality fusion) and/or multiple modalities processed using one or more techniques (inter-modality fusion). The context for data fusion in this investigation is to “measure” (i.e., assess and predict) corrosion-induced crack locations in aircraft lap joints. Pixel level multi-modal NDE data fusion techniques have been applied using probabilistic and wavelet methods [19, 20], and simple evidence theory as in [21]. Some NDE data fusion works involving fusing EC and UT measurement data have been outlined in [19, 22-25].

The first step in this investigation involved a comprehensive structural analysis process for identifying vulnerable regions in aircraft lap-joint mimics using eddy current NDE data only [11]. That study introduced a framework for systematic analysis of the test panels, from data collection to using this data for failure assessment of the test panels. The structural analysis process included quantizing and measuring characteristics of aluminum aircraft lap-joint mimics based on EC NDE data acquisition, defect detection and characterization, three-dimensional (3-D) structural model generation, finite-element modeling-based (FEM) simulation of fatigue damage for structural analysis [11]. This research extends the structural analysis process to multi-modal NDE data collection and intra- and inter-modal data fusion using image and signal processing and computational intelligence techniques for lap-joint mimic aircraft panel analysis.

Fusion of different NDE modalities (eddy current, millimeter-wave and ultrasonics) with complementary informational properties is performed to provide a comprehensive snapshot of the corrosion environment in these panels. This paper presents the comprehensive structural analysis process investigated based on models determined for different modality combinations for simulated fatigue testing for comparison with actual fatigue testing for five lap-joint mimic aircraft test panels.

## **II. METHODOLOGY**

### *A. Overview of Aircraft Lap-Joint Mimic Panel Description and Preparation*

A set of five aluminum lap-joint mimic test panels, four of which were corroded and one pristine, were used for the NDE data collection and data fusion-based measurement process. These panels were constructed using ten Al 2024-T3 aluminum plates with dimensions of 254 mm (10") by 76.2 mm (3") with a nominal thickness of 1.6 mm (0.063"). Two aluminum plates were stacked and riveted to create a lap-joint mimic test panel. Thus, ten aluminum plates produced five test panels. Prior to stacking and riveting, the aluminum plates of the corroded test panels were subjected to accelerated corrosion in a salt fog chamber following the ASTM B117 test standard. The ASTM B117 standard, designed in 1939, is a widely used technique for evaluating the relative corrosion of various metals and/or coatings. The salt spray chambers designed according to this standard are automated to maintain a specified environment within the chamber [26]. Details of the panel description and preparation have been reported in detail in [11]. Figure 1 shows one of each set of painted pristine and corroded panels, with the close-up views showing the riveted region of the panels.

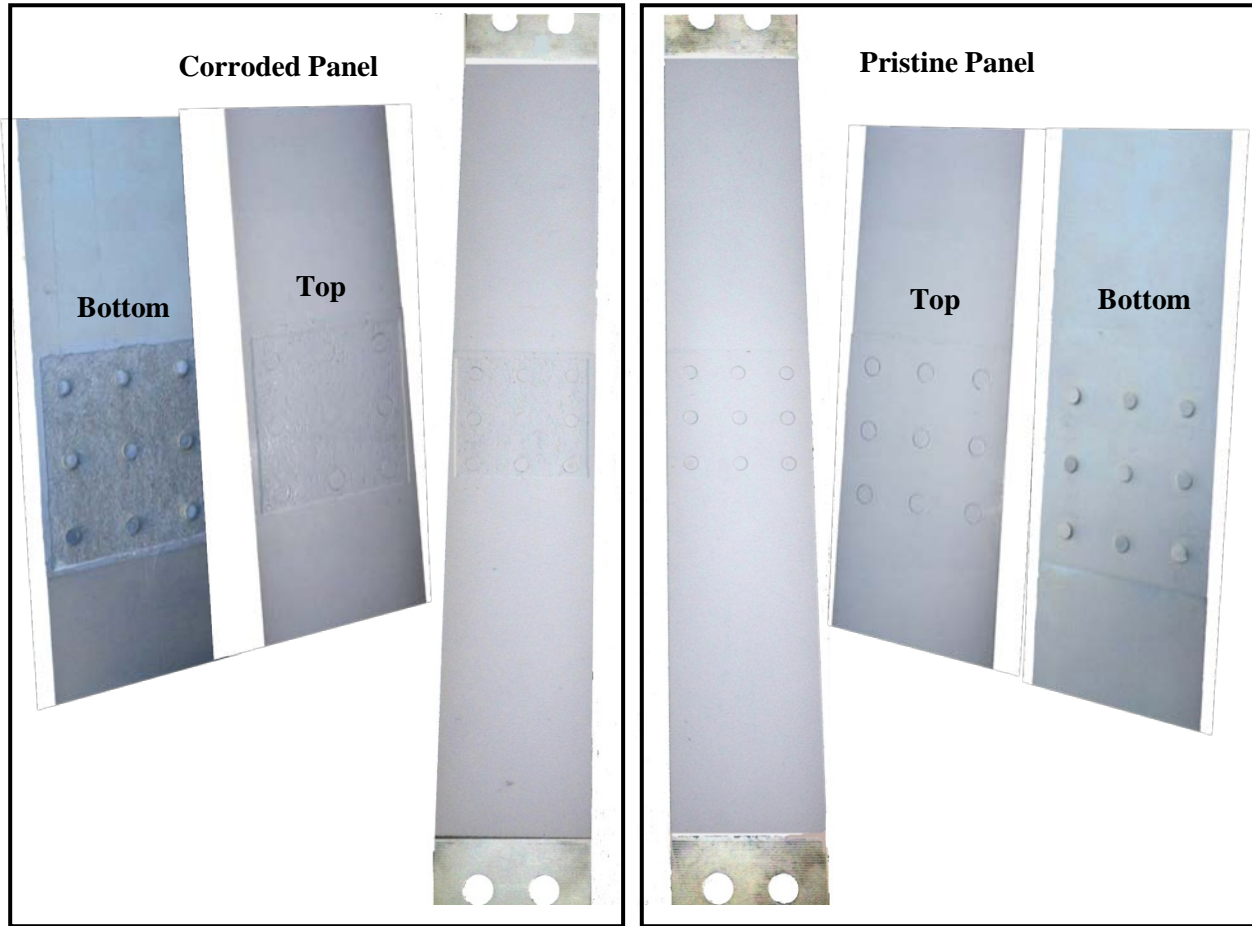


Figure 1: Picture of painted pristine and corroded panels with rivets.

### *B. Overview of NDE Data Collection and Test Panel Fatigue Testing*

For this investigation, three different NDE modalities were used; namely, EC, UT and MW methods. The test panels were subjected to two rounds of fatigue testing, with NDE data collected prior to each round. The fatigue testing was performed for comparison with the simulated fatigue loading analysis. During fatigue testing, the test panels were cyclically loaded between 1.04 kN and 10.4 kN (load ratio,  $R = P_{min}/P_{max} = 0.1$ ) at a frequency of 4 Hz. The calculated stress at the maximum load (10.4 kN) in the unriveted portions of the panels was 82.7 MPa. The first round of fatigue testing was intended to initiate small fatigue cracks, wherein, the

test panels were cyclically loaded until a crack was noticed (see Table 1). For the second round of fatigue testing, cracks were allowed to grow to twice their former lengths or if no cracks originated in the first round, cracks were initiated and allowed to grow to a length of ~3 mm. The panels were photographed using a stereomicroscope to inspect and measure crack lengths after each round. These cracks were meant to simulate in-service flaws. Details of the fatigue testing process (also referred to as the actual mechanical testing process), is provided in detail in [11]. Figure 2 shows the flowchart of the NDE data collection and fatigue testing steps for each round.

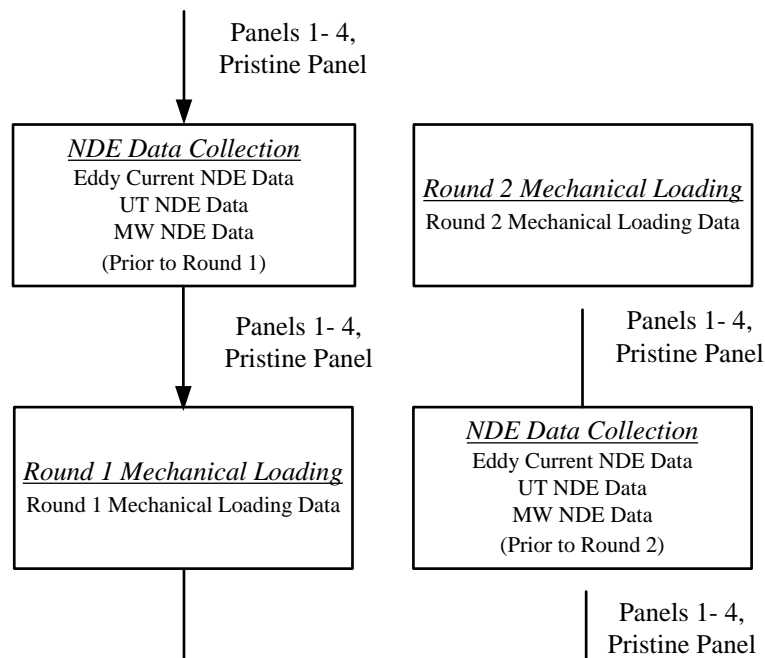


Figure 2: Flowchart of the NDE data collection and fatigue testing steps for each round.

### *C. Multi-Modal Data Fusion Process Overview*

Figure 3 presents the multi-modal NDE multi-modal comprehensive structural analysis process used in this study to detect test panel vulnerabilities, extending the previously investigated process involving only uni-modal EC NDE data [11]. The various steps in this comprehensive process consist of: 1) acquisition of NDE data for each modality, 2) acquisition of fatigue testing data, 3) intra-modal NDE data fusion for defect detection, 4) multi-modal fusion of the defect detection information, 5) defect characterization including material loss estimation, 6) 3-D model generation incorporating detected defects using the multi-modal data fusion approach, and 7) simulated fatigue testing for structural analysis and evaluation of the test panels with actual fatigue testing.

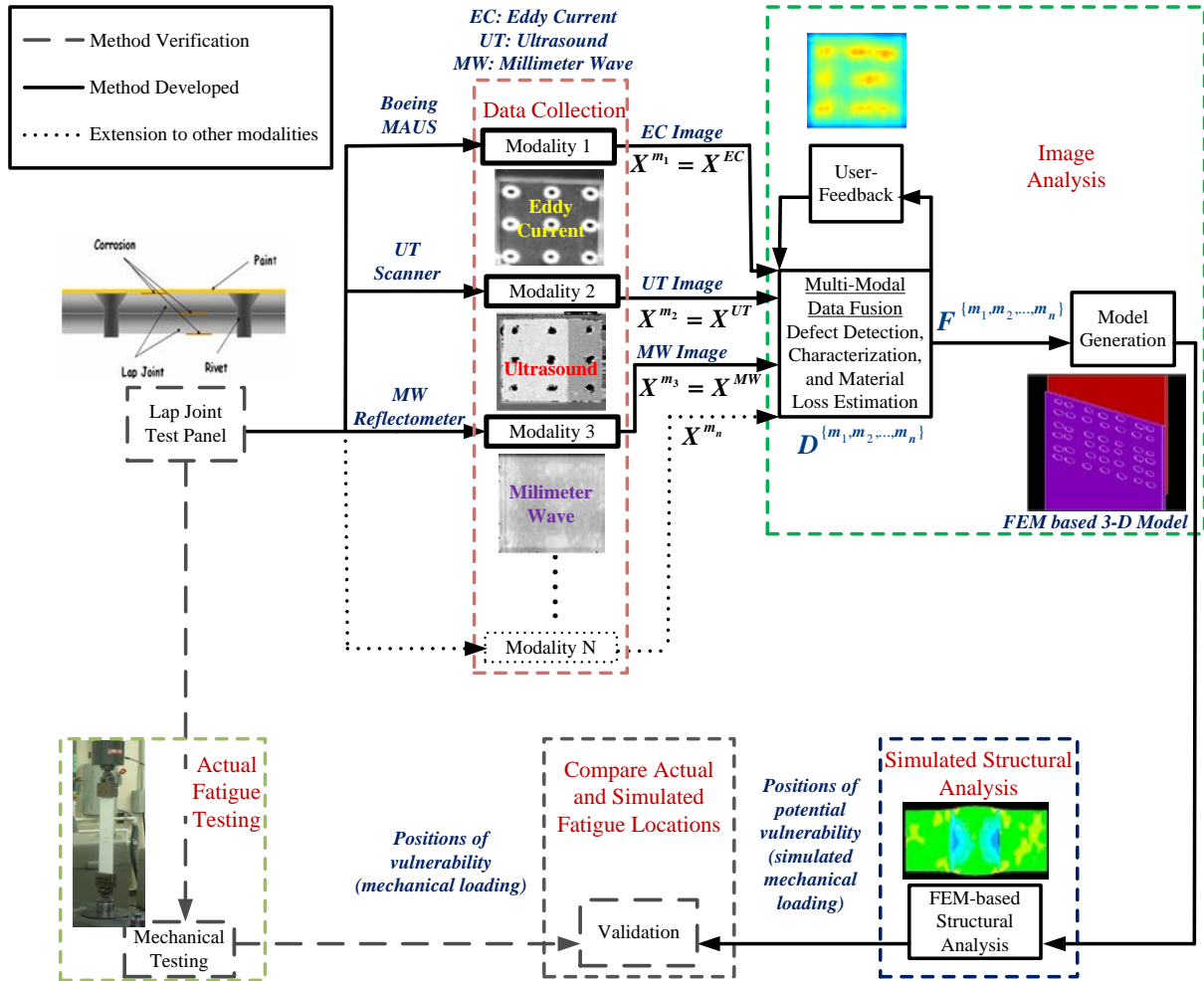


Figure 3: Overview of the multi-modal structural analysis process.

Let  $X^{m_1}, X^{m_2}, \dots, X^{m_n}$  denote the registered images obtained for each modality for a test panel (see Figures 3 and 4), where,  $m_1, m_2, \dots, m_n$  denote the  $n$  different modalities. Registering the different modality images for a test panel was performed by manually selecting the rivet positions, and an affine transformation was applied to generate images of standard size for the comprehensive structural analysis process (see Figure 3).

The next step in the process is corrosion detection. In the previous study, an Rx statistical method (Rx Detector) and a data-driven fuzzy logic-based (Fuzzy Detector) data fusion method was developed for corrosion detection [11, 27-29]. In [11], the data fusion method involved obtaining the decision-level fusion image (representing detected corrosion) from EC images only. In this study, a two-step data fusion approach was developed which can combine NDE data obtained from multiple modalities to create a final decision-level fusion image (see Figure 4). First, the multi-modal fusion between the results of the individual anomaly detectors (Rx and Fuzzy Detectors) was determined to create the fused detector level image. Second, the decision-level multi-modal fusion of the Rx and Fuzzy Detector images to produce the multi-modal decision-level fusion image.

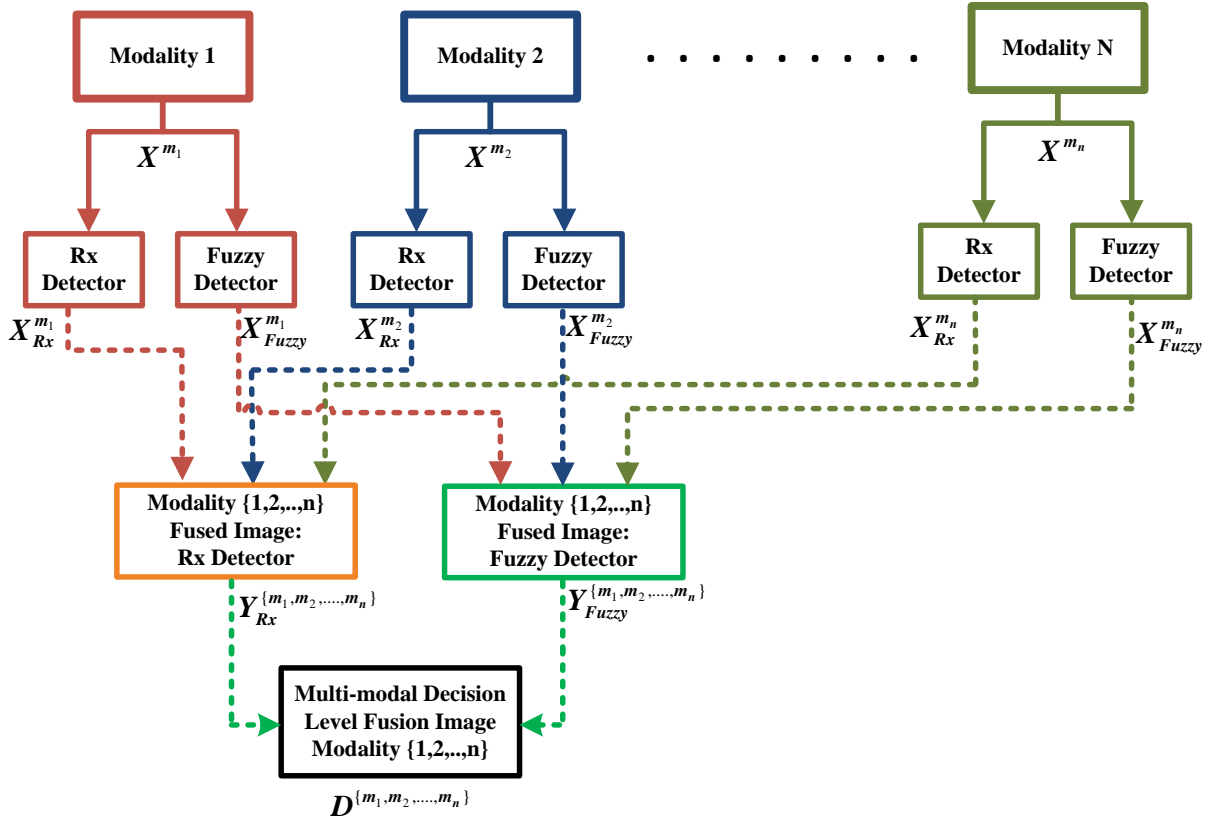


Figure 4: Various modality combinations used in the multi-modal corrosion detection algorithm

The Rx and Fuzzy detector images, as applied to the original modal images, are denoted as  $X_{Rx}^{m_1}, X_{Rx}^{m_2}, \dots, X_{Rx}^{m_n}$  and  $X_{Fuzzy}^{m_1}, X_{Fuzzy}^{m_2}, \dots, X_{Fuzzy}^{m_n}$ , respectively. The Rx and Fuzzy detector algorithms are given in detail in [11]. The next step involved the fusion of the detector images using a maximum-likelihood based method [30], which is given in Equations (1) and (2), where  $Y_{Rx}^{\{m_1, m_2, \dots, m_n\}}$  and  $Y_{Fuzzy}^{\{m_1, m_2, \dots, m_n\}}$  denote the fused Rx detector and Fuzzy detector images for the modality combination  $\{m_1, m_2, \dots, m_n\}$ , respectively, while  $\sigma_{Rx}^{m_1}, \sigma_{Rx}^{m_2}, \dots, \sigma_{Rx}^{m_n}$  and  $\sigma_{Fuzzy}^{m_1}, \sigma_{Fuzzy}^{m_2}, \dots, \sigma_{Fuzzy}^{m_n}$  denote the corresponding Rx and Fuzzy detector standard deviations from application to the original images, respectively.

$$Y_{Rx}^{\{m_1, m_2, \dots, m_n\}} = \frac{(\sigma_{Rx}^{m_1})^2 X_{Rx}^{m_1} + (\sigma_{Rx}^{m_2})^2 X_{Rx}^{m_2} + \dots + (\sigma_{Rx}^{m_n})^2 X_{Rx}^{m_n}}{(\sigma_{Rx}^{m_1})^2 + (\sigma_{Rx}^{m_2})^2 + \dots + (\sigma_{Rx}^{m_n})^2}, \quad (1)$$

$$Y_{Fuzzy}^{\{m_1, m_2, \dots, m_n\}} = \frac{(\sigma_{Fuzzy}^{m_1})^2 X_{Fuzzy}^{m_1} + (\sigma_{Fuzzy}^{m_2})^2 X_{Fuzzy}^{m_2} + \dots + (\sigma_{Fuzzy}^{m_n})^2 X_{Fuzzy}^{m_n}}{(\sigma_{Fuzzy}^{m_1})^2 + (\sigma_{Fuzzy}^{m_2})^2 + \dots + (\sigma_{Fuzzy}^{m_n})^2}, \quad (2)$$

Then,  $\sigma_{Rx}^{\{m_1, m_2, \dots, m_n\}}$  and  $\sigma_{Fuzzy}^{\{m_1, m_2, \dots, m_n\}}$  represent the standard deviation for the fused Rx and fused Fuzzy Detector images, respectively. Hence, the multi-modal decision-level fusion image is represented as  $D^{\{m_1, m_2, \dots, m_n\}}$ , and obtained as shown in Equation (3).

$$D^{\{m_1, m_2, \dots, m_n\}} = \frac{(\sigma_{Rx}^{\{m_1, m_2, \dots, m_n\}})^2 Y_{Rx}^{\{m_1, m_2, \dots, m_n\}} + (\sigma_{Fuzzy}^{\{m_1, m_2, \dots, m_n\}})^2 Y_{Fuzzy}^{\{m_1, m_2, \dots, m_n\}}}{(\sigma_{Rx}^{\{m_1, m_2, \dots, m_n\}})^2 + (\sigma_{Fuzzy}^{\{m_1, m_2, \dots, m_n\}})^2}, \quad (3)$$

Once the decision-level fusion image is obtained for corrosion detection, the next step in the comprehensive structural analysis process is to compute the material loss estimation image, denoted as  $F^{\{m_1, m_2, \dots, m_n\}}$  (see Figure 3). The material loss estimation image, as presented in detail in [23] is obtained using interpolation of cluster distance from known material loss signatures of 0%, 10%, 15% and 20% determined from a reference panel [11]. A sample schematic of a reference panel is shown in Figure 5.

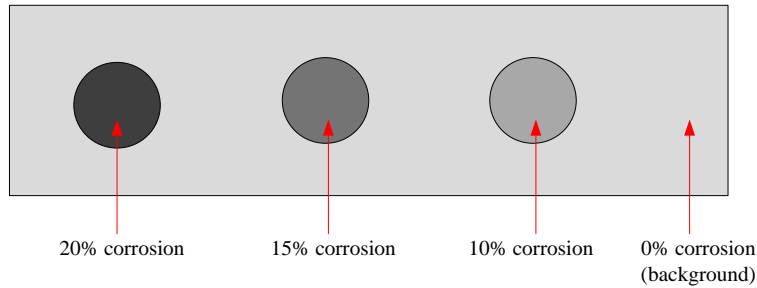


Figure 5: Sample schematic of a reference panel is used for the material loss estimation.

Using the material loss estimation technique explained above, a 3-D geometrical model representation for the riveted test panels is generated. A localized non-overlapping windowing method was used for model generation, presented in detail in [11].

### **III. NDE DATA ACQUISITION**

The process and sources of NDE data collected for the test panels and the actual fatigue testing process used for analyzing the test panels are presented in this section.

#### **B. PANEL DATA COLLECTION**

##### *1) Eddy Current Data*

To reveal corrosion/defects in the test panels, EC measurements were performed on each of the panels for two rounds of data collection. This data collection was performed at the Air Force Research Laboratory, OH, where images of the test panels were obtained from the painted side only since this is the accessible side on an aircraft. The EC data collection was performed using the Boeing MAUS<sup>®</sup> (Mobile Automated Scanner) raster scanning system, with phase lag adjustment to discern defect/corrosion depth. The inspected/imaged area covered the corroded regions containing the rivets, as shown in Figure 1. The details of the EC data collection are presented in detail in [11]. Figure 6 shows an example of such an EC data collection image.

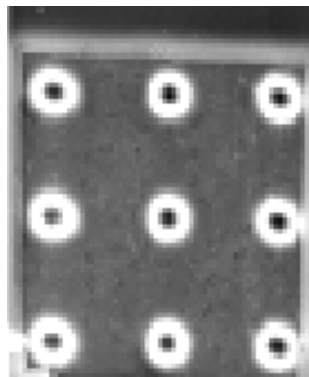


Figure 6: EC image of a corroded test panel.

## 2) Ultrasonics Data

Ultrasonics NDE data was also collected at the Air Force Research Laboratory, OH, in a similar fashion as those for EC. Measurements were conducted at a frequency of 15 MHz and images were produced using a step size of 0.015" [29]. As presented in Section II.A, each test panel comprises two aluminum plates, the top plate and the bottom plate. In Figure 1, the picture of the top and bottom sides of the test panel are shown. During the UT NDE data collection process, a reference panel image was obtained, representing 0%, 10%, 15%, and 20% material loss, as shown in Figure 7 (a). In Figure 7(a), physically, for example, the pixels contained in the 15% corrosion section represent 15% deviation from the pixels contained in the 0% corrosion region. These reference panel images were created to have baselines, representative of material loss in the test panels. They were primarily used for calibration purposes for corrosion detection and material loss estimation algorithm development. Figure 7(b) shows a UT image of the lap joint riveted region, as that used to produce the EC data shown in Figure 6.

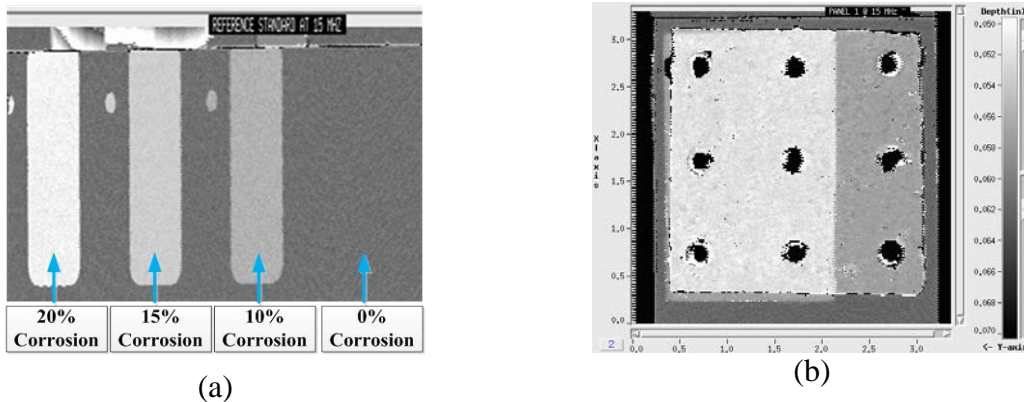


Figure 7: (a) Reference panel used for calibration purposes with areas of various levels of removed metal; (b) UT image of corroded test panel taken at 15 MHz.

## 3) Millimeter Wave Data

The MW images were produced at the Applied Microwave Nondestructive Testing Laboratory, Missouri S&T. A MW reflectometer, operating at 67 GHz (V-band) consisting of a

continuous-wave (CW) MW source (Gunn oscillator), a magic-tee (i.e., power splitter and combiner), and a diode detector was used, as shown in Figure 8. Through extensive measurements and considering trade-offs such as detection capability vs. spatial resolution, V-band (50-75 GHz) was shown to be a suitable frequency range for this investigation. As shown in Figure 8, a portion of the incident signal irradiates the sample through an open-ended rectangular waveguide probe with dimensions of 3.75 mm by 1.87 mm. The reflected signal is routed to the detector input. In addition, a portion of the incident signal is also routed to the detector input via a short circuit (e.g., reference signal) at the remaining port of the magic-tee. In this way the reflected and reference signals combine at the input to the detector. In this way, the detector behaves like a mixer and the detector's DC output voltage will be proportional to the magnitude and phase of the reflected signals. Given the small amount of expected corrosion, the phase of the reflected signal is mostly sensitive to the presence of corrosion. Subsequently, the lap joint panels were scanned by this reflectometer at certain standoff distance, producing MW images of the panels. These images in general are quite suitable for quantitative analysis, such as estimation of corrosion thickness, and data fusion with other modalities. Images were produced at 67 GHz for corroded and pristine panels corresponding to scanned areas of 80 mm by 55 mm, at step size of 2 mm by 1 mm, and at a standoff distance of 0.5 mm. These images were subsequently analyzed to determine the presence of corrosion and to evaluate corrosion thickness. It was found that the top 12 to 15 mm of each image consisted of non-corroded area, so that this information may be used as reference. Since the measurements were affected by the presence of sharp edges of the samples, using two polarizations (see Figure 9) yielded a better estimate of material loss. The technique for measuring the material loss (due to corrosion) is outlined in [15] in which a first order approximate model for the probe, not taking into account

multiple reflections, was developed. In this investigation, the parameters of the probe were directly measured using a performance network analyzer. Furthermore, the actual detector's input-output curve (from the datasheet) was used instead of assuming a square-law region of operation for more accurate model compared to [15]. As a result a relatively accurate model was obtained that converts a reflection coefficient at the aperture (5) (see Figure 8) of the probe to a voltage output at the detector. The theoretical reflection coefficient at the aperture of the probe was calculated using the model for open-ended waveguide radiating a multilayer structure (e.g., paint-corrosion-conductor) [16]. The dielectric constants of similar paint and corrosion layers were previously measured in [31]. Ultimately a curve was constructed relating the amount of corrosion/metal loss to the voltage output of the probe.

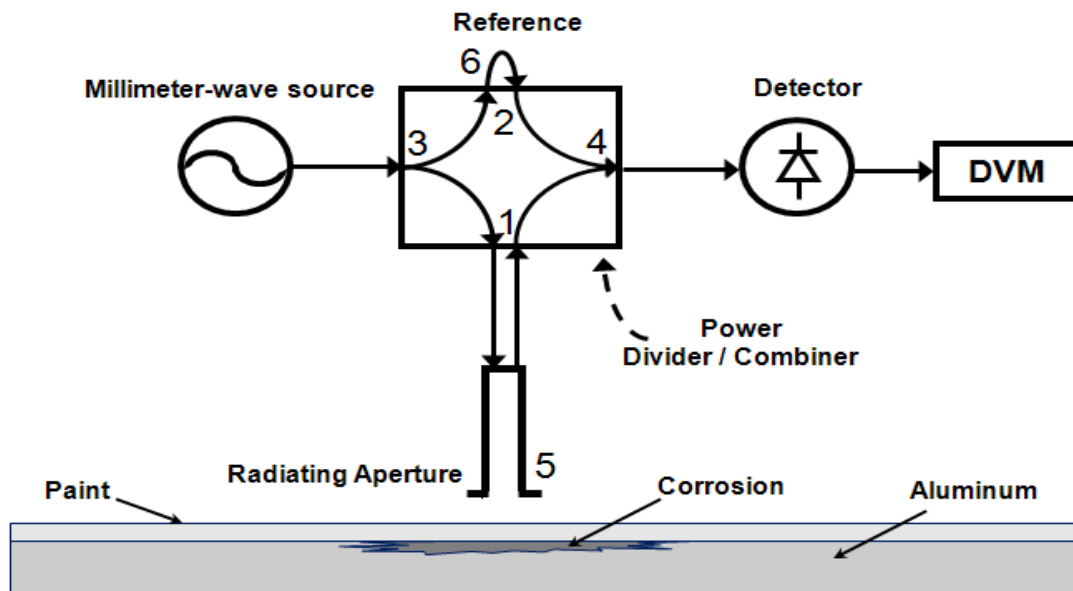


Figure 8: Schematic of the V-band millimeter wave reflectometer.

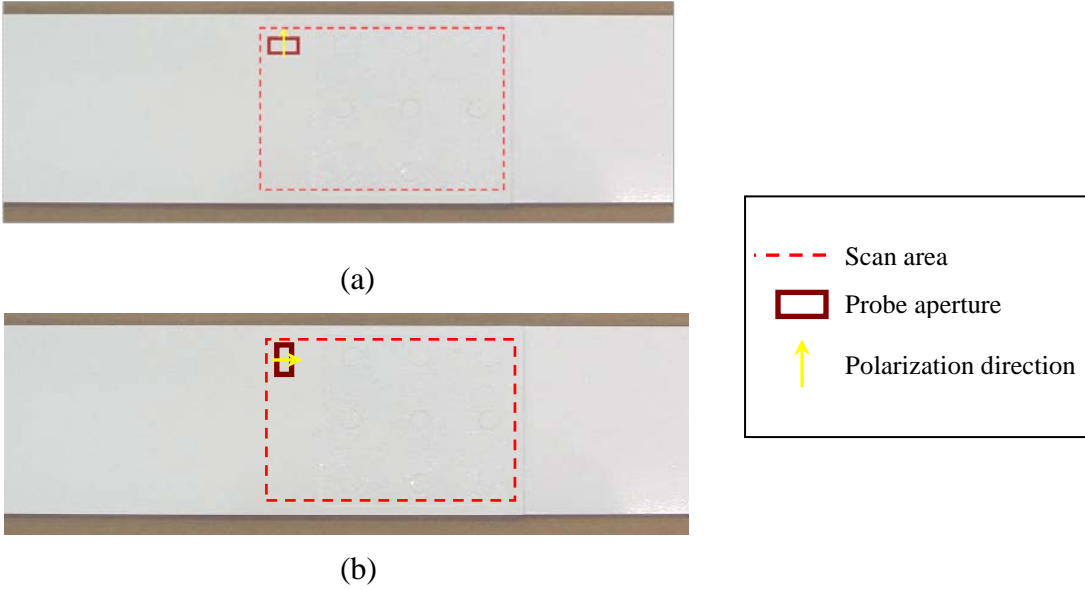


Figure 9: Picture of a sample with marked scanned area and orientation of probe aperture at (a) parallel and (b) perpendicular polarization.

The pixel value of every data point in these images is equal to the output voltage of the reflectometer at that particular location. For the MW images, each pixel location represented the thinning that occurred due to corrosion at that particular location. Therefore, the reference values for calibration purposes (analogous to reference panels explained earlier) to be used for material loss estimation was computed from the MW images directly using a scaling approach to find pixel values that would represent the 10%, 15% and 20% material loss areas in the MW images.

## B. MULTI-MODAL DATA FUSION ALGORITHMS

In this study, we investigated the multi-modal data fusion algorithm (presented in Section II.C) as applied to three separate multi-modal fusion cases:  $\{EC, UT\}$ ,  $\{EC, MW\}$  and,  $\{EC, UT, MW\}$ . If  $X^{EC}$ ,  $X^{UT}$  and  $X^{MW}$  denote the images that are obtained using the three different modalities, then  $X_{Rx}^{EC}$ ,  $X_{Rx}^{UT}$  and  $X_{Rx}^{MW}$  Let  $X_{Rx}^{EC}$ ,  $X_{Rx}^{UT}$  and  $X_{Rx}^{MW}$  represent the Rx Detector images of the EC, UT and MW modalities, respectively. Similarly,  $X_{Fuzzy}^{EC}$ ,  $X_{Fuzzy}^{UT}$  and

$X_{Fuzzy}^{MW}$  represent the corresponding Fuzzy Detector images. Then, the fused Rx Detector images are represented as  $Y_{Rx}^{\{EC,UT\}}$ ,  $Y_{Rx}^{\{EC,MW\}}$  and  $Y_{Rx}^{\{EC,UT,MW\}}$  (Equations (4)-(6)) for the  $\{EC,UT\}$ ,  $\{EC,MW\}$  and,  $\{EC,UT,MW\}$  cases.

$$Y_{Rx}^{\{EC,UT\}} = \frac{(\sigma_{Rx}^{EC})^2 X_{Rx}^{EC} + (\sigma_{Rx}^{UT})^2 X_{Rx}^{UT}}{(\sigma_{Rx}^{EC})^2 + (\sigma_{Rx}^{UT})^2} \quad (4)$$

$$Y_{Rx}^{\{EC,MW\}} = \frac{(\sigma_{Rx}^{EC})^2 X_{Rx}^{EC} + (\sigma_{Rx}^{MW})^2 X_{Rx}^{MW}}{(\sigma_{Rx}^{EC})^2 + (\sigma_{Rx}^{MW})^2} \quad (5)$$

$$Y_{Rx}^{\{EC,UT,MW\}} = \frac{(\sigma_{Rx}^{EC})^2 X_{Rx}^{EC} + (\sigma_{Rx}^{UT})^2 X_{Rx}^{UT} + (\sigma_{Rx}^{MW})^2 X_{Rx}^{MW}}{(\sigma_{Rx}^{EC})^2 + (\sigma_{Rx}^{UT})^2 + (\sigma_{Rx}^{MW})^2} \quad (6)$$

Similarly, the fused Fuzzy Detector images are represented as  $Y_{Fuzzy}^{\{EC,UT\}}$ ,  $Y_{Fuzzy}^{\{EC,MW\}}$  and  $Y_{Fuzzy}^{\{EC,UT,MW\}}$  (Equations (7)-(9)).

$$Y_{Fuzzy}^{\{EC,UT\}} = \frac{(\sigma_{Fuzzy}^{EC})^2 X_{Fuzzy}^{EC} + (\sigma_{Fuzzy}^{UT})^2 X_{Fuzzy}^{UT}}{(\sigma_{Fuzzy}^{EC})^2 + (\sigma_{Fuzzy}^{UT})^2} \quad (7)$$

$$Y_{Fuzzy}^{\{EC,MW\}} = \frac{(\sigma_{Fuzzy}^{EC})^2 X_{Fuzzy}^{EC} + (\sigma_{Fuzzy}^{MW})^2 X_{Fuzzy}^{MW}}{(\sigma_{Fuzzy}^{EC})^2 + (\sigma_{Fuzzy}^{MW})^2} \quad (8)$$

$$Y_{Fuzzy}^{\{EC,UT,MW\}} = \frac{(\sigma_{Fuzzy}^{EC})^2 X_{Fuzzy}^{EC} + (\sigma_{Fuzzy}^{UT})^2 X_{Fuzzy}^{UT} + (\sigma_{Fuzzy}^{MW})^2 X_{Fuzzy}^{MW}}{(\sigma_{Fuzzy}^{EC})^2 + (\sigma_{Fuzzy}^{UT})^2 + (\sigma_{Fuzzy}^{MW})^2} \quad (9)$$

The decision-level fusion images were obtained utilizing the detector level fusion images using the same maximum likelihood scheme defined earlier [30]. Extending Equation (3) for the EC, UT and MW modalities, the decision-level fusion images for the multi-modal case is

mathematically expressed by  $D^{\{EC,UT\}}$ ,  $D^{\{EC,MW\}}$  and  $D^{\{EC,UT,MW\}}$  as shown in Equations (10)-(12), for the  $\{EC,UT\}$ ,  $\{EC,MW\}$  and,  $\{EC,UT,MW\}$  modality combinations, respectively.

$$D^{\{EC,UT\}} = \frac{(\sigma_{Rx}^{\{EC,UT\}})^2 Y_{Rx}^{\{EC,UT\}} + (\sigma_{Fuzzy}^{\{EC,UT\}})^2 Y_{Fuzzy}^{\{EC,UT\}}}{(\sigma_{Rx}^{\{EC,UT\}})^2 + (\sigma_{Fuzzy}^{\{EC,UT\}})^2}, \quad (10)$$

$$D^{\{EC,MW\}} = \frac{(\sigma_{Rx}^{\{EC,MW\}})^2 Y_{Rx}^{\{EC,MW\}} + (\sigma_{Fuzzy}^{\{EC,MW\}})^2 Y_{Fuzzy}^{\{EC,MW\}}}{(\sigma_{Rx}^{\{EC,MW\}})^2 + (\sigma_{Fuzzy}^{\{EC,MW\}})^2}, \quad (11)$$

$$D^{\{EC,UT,MW\}} = \frac{(\sigma_{Rx}^{\{EC,UT,MW\}})^2 Y_{Rx}^{\{EC,UT,MW\}} + (\sigma_{Fuzzy}^{\{EC,UT,MW\}})^2 Y_{Fuzzy}^{\{EC,UT,MW\}}}{(\sigma_{Rx}^{\{EC,UT,MW\}})^2 + (\sigma_{Fuzzy}^{\{EC,UT,MW\}})^2}, \quad (12)$$

A material loss estimation image was computed for each of the decision-level fusion images for the different modality combinations. The material loss estimation presented in detail in [29], produces the final material loss estimation images,  $F^{\{EC,UT\}}$ ,  $F^{\{EC,MW\}}$  and  $F^{\{EC,UT,MW\}}$  for the various modality combinations  $\{EC,UT\}$ ,  $\{EC,MW\}$  and,  $\{EC,UT,MW\}$  respectively. Examples of material loss estimation images are shown in Figure 13.

### C. 3-D MODEL GENERATION AND FATIGUE TESTING OF THE PANELS

ANSYS<sup>®</sup> was to perform the simulated fatigue testing based on the 3-D model of the panel. The simulated fatigue testing process is presented in the next section.

## IV. EXPERIMENTAL RESULTS

### A. MULTI-MODAL DATA FUSION EXPERIMENTS

The NDE data collected from the three modalities were subjected to the RX and Fuzzy detectors and then to the decision-level fusion process, the details of which have been explained in Section III.B. Experimental results for the raw EC, UT and MW images, with their respective material

loss estimation images are shown in Figures 10-12, with the reference scale for material loss estimation between 0% and 20% are presented for corroded test panel 1. Figure 10 presents EC testing data prior to round 1 of actual fatigue testing [11], Figure 11 presents the UT data and Figure 12 shows the MW data.

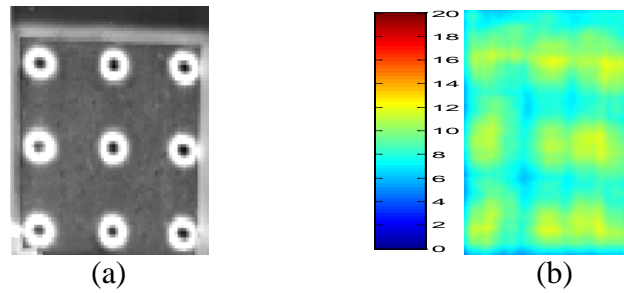


Figure 10: Data collected and data fusion based material loss estimation algorithm results for test panel 1 prior to round 1 of actual fatigue testing. (a) EC data for test panel 1, (b) material loss estimation map with reference scale [11] .

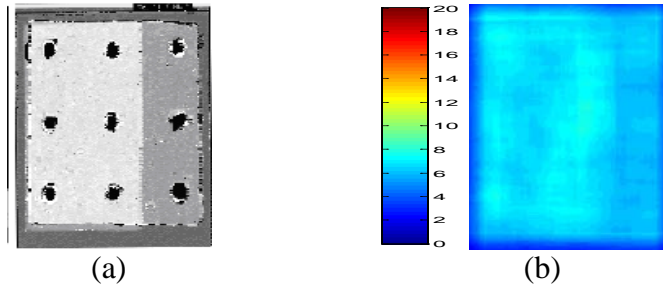


Figure 11: Data collected and data fusion based material loss estimation algorithm results for test panel prior to round 1 of actual fatigue testing. (a) UT data for test panel 1, (b) material loss estimation map with reference scale.

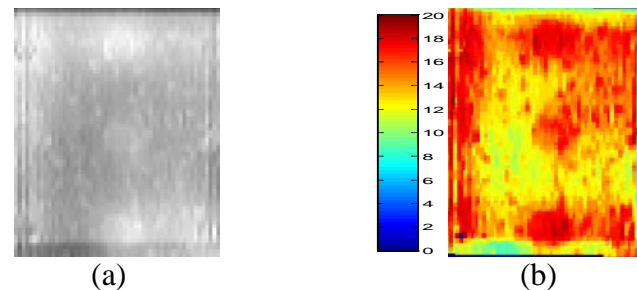


Figure 12: Data collected and data fusion based material loss estimation algorithm results for test panel 1 prior to round 1 of actual fatigue testing. (a) MW data for test panel 1, (b) material loss estimation map with reference scale.

The material loss estimation images using the data fusion method for the individual modalities were performed so that the results could be compared to the multi-modal data fusion-based material loss estimation method. Once the material loss estimation results for all three modalities were obtained, the multi-modal data fusion algorithm explained in Section III.B was used to obtain the material loss estimation images. For test panel 1, Figure 13(a) shows the EC and UT fused results, Figure 13(b) shows the EC and MW fused results while the EC, UT and MW fused results for the NDE data obtained prior to the first round of actual mechanical testing are shown in Figure 13(c).

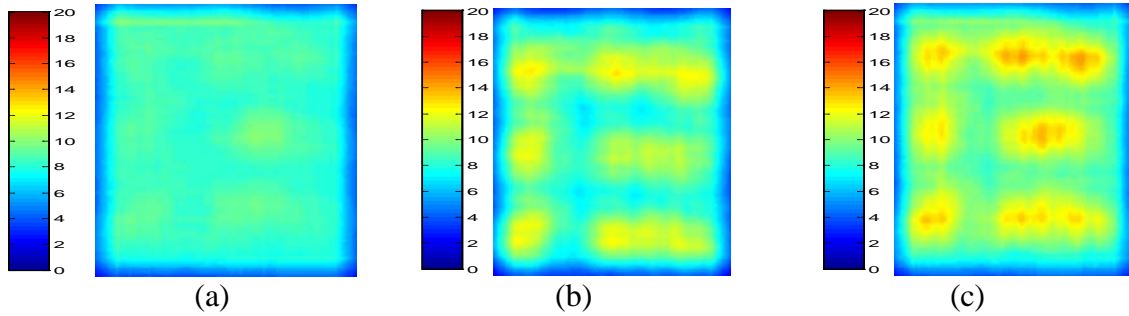


Figure 13: Multi-modal data fusion based material loss estimation results for panel 1 for NDE data obtained prior to round 1 of fatigue testing. (a) EC and UT fused result, (b) EC and MW fused result, (c) EC, UT and MW fused result.

Material loss estimation results obtained from the above cases using the individual modalities and also the multi-modal data fusion approach were analyzed with respect to the actual experimental results. The average material loss was computed over the non-zero corrosion areas in the material loss estimation results obtained using each of the three NDE modalities, EC (Figure 11(c)), UT (Figure 12(c)) and MW (Figure 13(c)) and also from the fused modalities, EC and UT (Figure 14(a)), EC and MW (Figure 15(b)) and EC, UT and MW (Figure 14(c)). The average material losses of test panel 1 as obtained from the various modalities and also from the fusion of the modalities are shown in Table 1.

Table 1: Summary of material loss estimation results using uni- and multi-modal data fusion for NDE data obtained prior to first round of mechanical testing

Modality	Material Loss Estimation (%)
EC	13
UT	17.1 (top scan only)
MW	16.3 (top scan only)
$\{EC, UT\}$	14.2
$\{EC, MW\}$	14.7
$\{EC, UT, MW\}$	17.4

In previous research test panel 1 showed an actual average material loss of 16-17% over the entire panel [29], compared to the material loss estimated based on comprehensive structural analysis process for different modality combinations given in Table 1. The UT scan denotes a 17.1% average material loss for test panel 1, which is similar to the EC, UT and MW fused result (17.4%). It is important to mention here that the UT data depicts the material loss present in the top layer of the panel, which does not represent the material loss of the entire panel since corrosion exists in both the top and bottom layer of the panels (see Figure 1). The MW images also provide corrosion/material loss information for the top layer of the test panels only. In order to evaluate the average material loss over the entire panel, the EC images, which provide depth information at the various layers within the panel, were fused with the other modalities to obtain a more comprehensive material loss evaluation.

## B. ACTUAL FATIGUE TESTING RESULTS FOR TEST PANELS

During the actual fatigue testing of the panels we observed that all of the cracks developed on the lower row of rivets, suggesting a higher stress concentration at this row. Table 2 presents a

summary of the actual fatigue testing crack locations across the two rounds of mechanical testing, the details of which can be found in [11]. These results are used for comparison purposes with the crack locations predicted by the data fusion based simulated fatigue testing process using FEM structural modeling and analysis. For reference purposes, a schematic outlining the various rounds of the NDE data collection and mechanical loading process is provided in Figure 2 for the different panels.

Table 2: Summary of crack locations for the two rounds of fatigue loading. Refer to Figure 15 for test panel location key.

Panel #	Crack locations found after Round 1	Cracks locations found after Round 2
1	13, 15	13, 15
2	13	13, 14
3	None	14
4	None	14
6	13, 16	13, 14, 16

### C. 3-D MODEL GENERATION FOR SIMULATED FATIGUE TESTING

A 3-D geometrical model for the riveted test panels was generated based on a localized non-overlapping window method using a material loss estimate map of a given test panel. The method divided the height and width dimensions of the test panel into 10x10 (approximately 5 mm x 5 mm) non-overlapping windows. The average material loss over a non-overlapping window was estimated, and the 3-D center of mass was computed. A circular puck-like region was created with a thickness equal to the average material loss of the window, and area equal to the number of non-zero pixels (indicating corrosion and thus material loss) present in the window. This circular puck-like region was then centered within the non-overlapping window.

This method was repeated for all non-overlapping windows in each panel. Such a 3-D model obtained for test panel 1 for the  $\{EC, UT, MW\}$  modality combination is shown in Figure 14, illustrated using ANSYS®. Note that the puck-like regions shown in Figure 14 are actually solid material loss regions, which could not be visually represented using the ANSYS® display tool. Also, note that the 3-D modeling method was developed based on constraints in ANSYS®, which is used for simulated fatigue loading of the test panels.

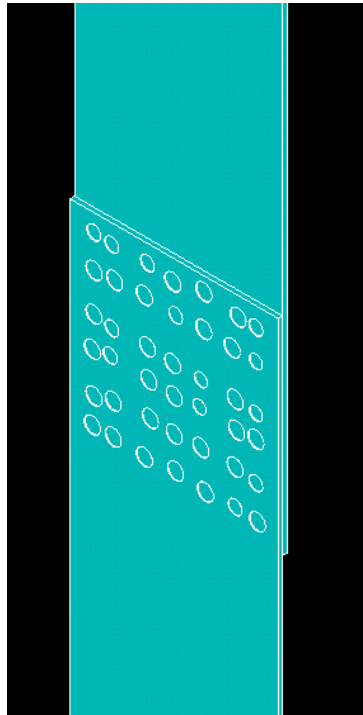


Figure 14: Model generation for a test panel using localized non-overlapping window method, displayed using ANSYS® for test panel 1 for the  $\{EC, UT, MW\}$  modality combination.

### C. SIMULATED FATIGUE TESTING RESULTS

As part of the comprehensive structural analysis process, the simulated fatigue testing process using ANSYS was performed. The riveted regions in the test panel 3D models were marked and the displacements with respect to each layer were set to zero to simulate the actual riveted

structure of the panels. After the riveted regions were marked and their displacement set to zero for all directions at these regions, the boundary conditions applied to the panel during simulated loading were setup to simulate the actual mechanical loading. In the actual fatigue testing, the test panel was subjected to a fixed load on the top and an actuator at the bottom to facilitate the cyclical loading of the panel. Details of the actual fatigue testing are provided in [11].

Alternating Stress Intensity (Alt-SI) values for all the nodes of the meshed panel were determined using the Fatigue Analysis module in ANSYS® as a measure of the vulnerability of a specific node/region for failure. In general, evaluating the results of the simulated structural analysis of the test panels, it was observed that some locations had significantly higher stress concentration (Alt-SI) as compared to the entire panel. These panel locations were designated as the critical locations of the panel (locations 13-18), as shown in from Figure 15. Based on this, locations 1-12 are designated as the non-critical panel locations.

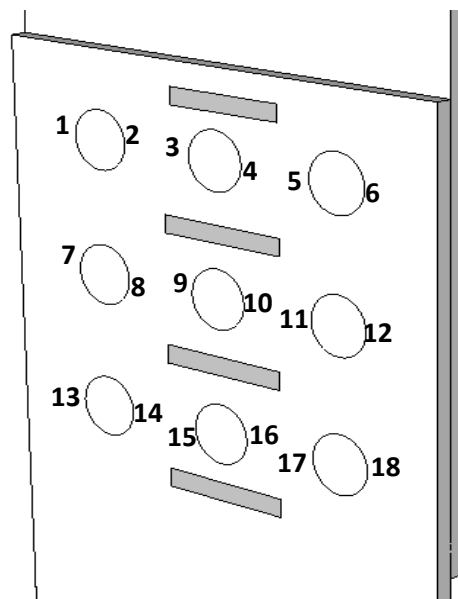


Figure 15: Location key (critical and non-critical locations) for crack initiation sites in test panels.

Table 3: Summary of Alt-SI values for test panel 1 for the two rounds of simulated fatigue testing using multi-modal data fusion results.

	Before round 1 of actual testing			After round 1 of actual testing		
	{EC,UT} (MPa)	{EC,MW} (MPa)	{EC,UT,MW} (MPa)	{EC,UT} (MPa)	{EC,MW} (MPa)	{EC,UT,MW} (MPa)
<b>Location 1</b>	3.2	2.7	2.2	5.5	4.7	8.1
<b>Location 2</b>	0.2	1.3	0.8	1.0	0.6	0.3
<b>Location 3</b>	0.7	1.0	0.6	1.1	0.5	0.2
<b>Location 4</b>	0.5	1.3	0.4	0.7	0.5	0.2
<b>Location 5</b>	0.2	1.3	0.6	1.0	0.3	0.0
<b>Location 6</b>	3.9	2.2	3.5	5.5	9.7	6.4
<b>Location 7</b>	28.7	28.0	8.5	6.8	2.2	2.5
<b>Location 8</b>	1.1	0.8	4.5	3.7	3.0	1.2
<b>Location 9</b>	2.1	6.5	4.3	3.8	5.0	1.7
<b>Location 10</b>	0.4	1.0	3.0	3.6	4.8	0.8
<b>Location 11</b>	2.7	1.4	5.9	2.8	1.5	1.2
<b>Location 12</b>	4.8	5.0	4.0	21.0	5.1	0.8
<b>Location 13</b>	134.9	109.3	83.6	55.6	84.1	76.9
<b>Location 14</b>	72.9	63.2	70.5	108.1	67.5	45.0
<b>Location 15</b>	57.5	75.9	55.0	70.7	64.6	51.9
<b>Location 16</b>	33.2	92.7	21.1	46.5	54.5	47.4
<b>Location 17</b>	9.2	63.5	35.3	55.4	47.9	36.0
<b>Location 18</b>	40.0	34.7	37.4	45.4	54.8	43.3

Furthermore, the crack locations identified during the actual fatigue testing (Table 1) exhibited no cracks in the test panels at locations 1-12. All the detected cracks were between locations 13-18. Table 3 gives the Alt-SI values for the different locations from Figure 15 for test panel 1 for

different modality combinations. Similar data tables were generated for test panels 1-4 and the pristine panel. Table 4 presents the Alt-SI values for test panels 1-4 and the pristine panel for the  $\{EC, UT\}$  modality combination.

Table 4: Summary of Alt-SI values for test panels 1-4 and pristine panel for the two rounds of simulated fatigue testing using multi-modal data fusion:  $\{EC, UT\}$ .

	Before round 1 of actual testing (in MPa)					After round 1 of actual testing (in MPa)				
	Test Panel 1	Test Panel 2	Test Panel 3	Test Panel 4	Pristine Panel	Test Panel 1	Test Panel 2	Test Panel 3	Test Panel 4	Pristine Panel
Location 1	3.2	0.8	3.4	1.3	1.5	5.5	2.3	9.1	10.0	12.7
Location 2	0.2	0.5	4.6	2.3	1.0	1.0	0.4	0.7	0.5	2.0
Location 3	0.7	0.4	4.2	3.3	0.7	1.1	0.4	0.5	0.5	1.7
Location 4	0.5	0.5	6.0	1.7	0.2	0.7	0.3	0.4	0.7	1.2
Location 5	0.2	0.6	5.5	2.3	0.5	1.0	0.1	0.1	0.2	0.3
Location 6	3.9	2.0	2.4	18.8	1.1	5.5	8.0	1.4	9.1	1.6
Location 7	28.7	4.8	6.8	33.4	5.8	6.8	11.5	9.7	24.3	3.0
Location 8	1.1	3.3	3.5	8.8	3.5	3.7	2.3	1.6	3.9	4.4
Location 9	2.1	2.0	10.9	9.2	1.4	3.8	2.4	2.0	4.0	4.3
Location 10	0.4	0.4	0.9	7.4	4.1	3.6	11.4	3.1	4.9	4.0
Location 11	2.7	1.6	2.6	6.3	5.5	2.8	1.7	2.2	3.0	4.5
Location 12	4.8	1.7	3.9	6.4	5.4	21.0	5.1	3.6	6.1	34.1
Location 13	134.9	44.0	48.7	56.2	50.1	55.6	73.0	32.9	49.4	92.8
Location 14	72.9	35.6	33.3	55.4	1.0	108.1	58.2	110.9	56.7	60.8
Location 15	57.5	39.3	53.6	51.4	34.2	70.7	47.0	56.6	49.0	49.1
Location 16	33.2	26.2	31.3	55.8	34.5	46.5	43.1	39.7	49.3	67.1
Location 17	9.2	26.1	36.5	53.2	13.2	55.4	42.1	50.1	53.9	46.2
Location 18	40.0	53.0	49.6	51.1	24.6	45.4	56.3	53.2	61.7	59.5

A fuzzy-set approach was used to find the cutoff value for automatic detection of the cracks from the Alt-SI values of the simulated fatigue testing of the panels. A fuzzy set  $\mathbf{P}$  provides the degree of vulnerability in a structure (test and pristine panels) at a specified position in terms of Alt-SI. Let  $\mu_p(V)$  represents the membership value in  $\mathbf{P}$  for an Alt-SI value,  $V$ , determined in a structure at a specified position.  $\mu_p(V)$  is defined in equation (13):

$$\mu_p(V) = \begin{cases} \frac{V}{70}, & \text{if } Alt - SI < 70 \text{ MPa} \\ 1, & \text{otherwise} \end{cases} \quad (13)$$

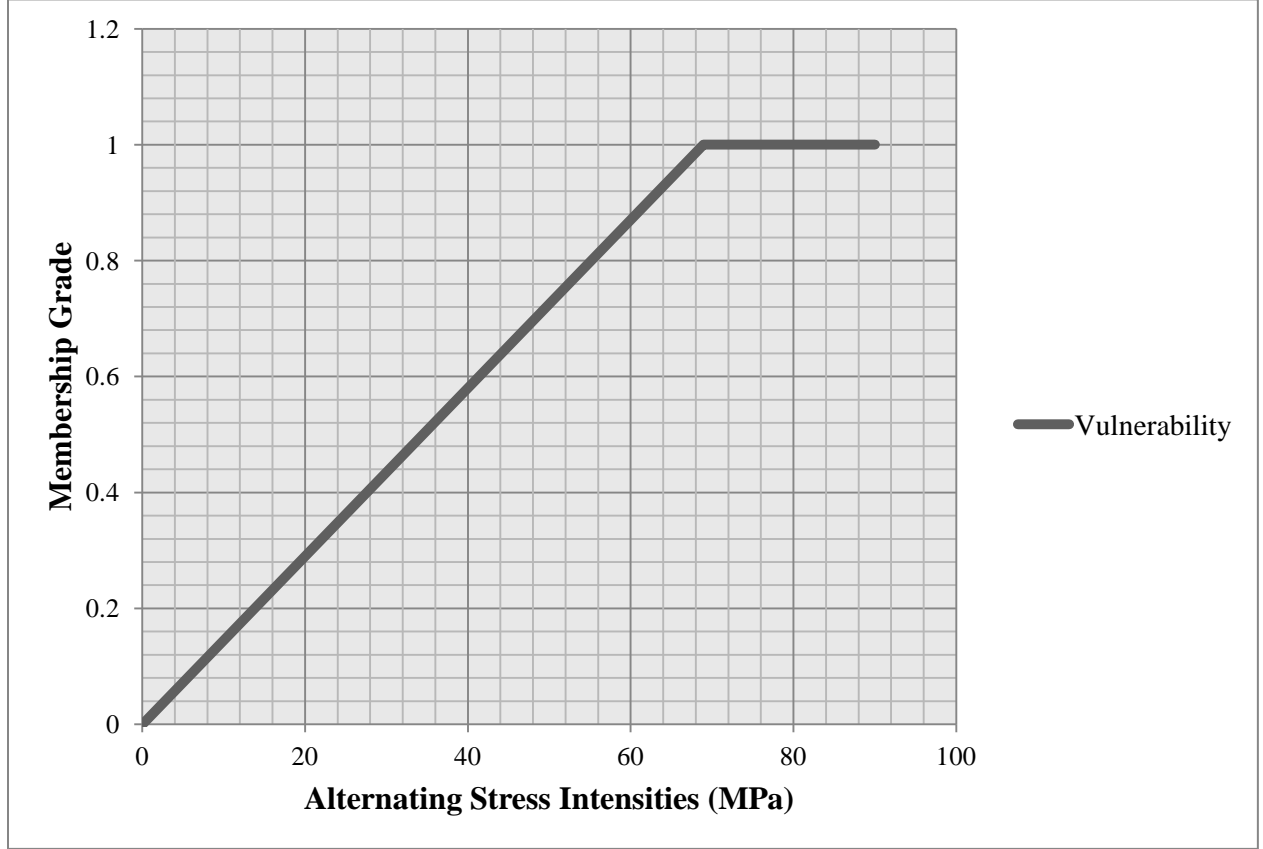


Figure 16: Fuzzy-logic based method of automatically finding the threshold for crack prediction.

Figure 16 shows the membership function  $\mu_p(V)$ . Alpha-cuts ( $\alpha$ ) on the fuzzy set  $P$  were examined for determining test panel vulnerability positions, where all positions with  $\mu_p(V) \geq \alpha$  are designated as vulnerable for  $0 \leq \alpha \leq 1$  as shown in Equation 14.

$$\text{Vulnerability} = \begin{cases} 1, & \text{if } \mu_p(V) \geq \alpha \\ 0, & \text{otherwise} \end{cases} \text{ for } 0 \leq \alpha \leq 1 \quad (14)$$

An alpha-cut value of 0.45 ( $\alpha = 0.45$ ) produced the best results, the details of which for each test panel and each modality combination for all the two rounds of simulated fatigue testing are

summarized in Table 5. True positive and true negative crack location detection rates were computed over the four corroded and one pristine test panels. A true positive crack location is correctly labeled if the location satisfies the Alt-SI threshold constraint, and the location in the test panel for the corresponding round of mechanical loading is designated as a crack site, as given in Table 2. A true negative location is labeled correctly if the location does not satisfy the Alt-SI threshold constraint, and the location in the test panel for the corresponding round of mechanical loading is not called a crack site, as shown in Table 2. False positives are the number of cracks that were erroneously detected across all panels, and false negatives refer to cases when the simulated fatigue loading method failed to predict a crack location that was actually a crack location obtained by the mechanical loading process. For each round of testing, and for each modality combination, 18 total number of true positive and true negative locations resulted. In Table 5, the number on the left side of the slash indicates the number of vulnerable locations (true positive) and the number of non-vulnerable locations (true negative) found from the simulated fatigue testing process, and the number to the right of the slash gives the true positive and true negative locations as found from actual fatigue testing.

Table 5: Accuracy metrics of simulated testing v/s mechanical testing. Number of locations found using simulated fatigue testing/number of locations using actual fatigue testing.

	Before round 1 of actual testing						After round 1 of actual testing					
	True Positive			True Negative			True Positive			True Negative		
	{EC,UT}	{EC,MW}	{EC,UT,MW}	{EC,UT}	{EC,MW}	{EC,UT,MW}	{EC,UT}	{EC,MW}	{EC,UT,MW}	{EC,UT}	{EC,MW}	{EC,UT,MW}
<b>Panel 1</b>	2/2	2/2	2/2	14/16	12/16	13/16	2/2	2/2	2/2	12/16	12/16	12/16
<b>Panel 2</b>	1/1	1/1	1/1	17/17	17/17	17/17	2/2	2/2	2/2	16/16	16/16	16/16
<b>Panel 3</b>	0/0	0/0	0/0	18/18	18/18	18/18	1/1	1/1	1/1	17/17	17/17	17/17
<b>Panel 4</b>	0/0	0/0	0/0	18/18	18/18	18/18	1/1	1/1	1/1	17/17	17/17	17/17
<b>pristine</b>	2/2	2/2	1/2	16/16	16/16	16/16	3/3	2/3	1/3	15/15	15/15	15/15
<b>Total</b>	5/5	5/5	4/5	83/85	81/85	82/85	9/9	8/9	7/9	77/81	77/81	77/81

The accuracy for each round of simulated fatigue testing is computed by calculating the sum of true positives and true negatives detected divided by the total number of positions for each round of the fatigue testing. Table 6 shows the summarized results obtained using this method. From [11], the EC only data the correct prediction rates were as high as 88.9% for the rounds of simulated fatiguing, with an average correct prediction rate of 87.8%. For the multi-modal fused data, the correct prediction rate was as high as 98.8% for the  $\{EC, UT\}$  case before round 1 of actual mechanical testing. For each round of simulated fatigue testing, the Average Accuracy was computed by averaging the Overall Accuracies for the different modality combinations. As shown in Table 6, the average correct prediction rates before the first round of actual testing and after the first round of actual testing are 95.0% and 92.0%, respectively. In general, the data fusion process yielded a consistent correlation for vulnerability location compared to visual inspection from actual fatigue testing.

Table 6: Summary of accuracy estimates obtained using information from Table 5.

	{EC,UT}			{EC,MW}			{EC,UT,MW}		
	True Positive	True Negative	Overall Accuracy	True Positive	True Negative	Overall Accuracy	True Positive	True Negative	Overall Accuracy
<b>Before round 1 of actual testing</b>	100.0%	97.6%	<b>98.8%</b>	100.0%	95.3%	<b>97.7%</b>	80.0%	96.5%	<b>88.2%</b>
<b>Average Accuracy</b>	$(98.8+97.7+88.2)/3=95.0\%$								
<b>After round 1 of actual testing</b>	100.0%	95.1%	<b>97.5%</b>	88.9%	95.1%	<b>92.0%</b>	77.8%	95.1%	<b>86.5%</b>
<b>Average Accuracy</b>	$(97.5+92+86.5)/3=92.0\%$								

## V. DISCUSSION

From Figure 13 for test panel 1, the modality combination  $\{EC, UT, MW\}$  visually detects greater corrosion (i.e., more material loss), compared to the  $\{EC, UT\}$  and  $\{EC, MW\}$  combinations. The results in Table 5 for test panel 1 show that the same vulnerable locations (see Figure 15) were found for the  $\{EC, UT\}$ ,  $\{EC, MW\}$ , and  $\{EC, UT, MW\}$  combinations based on the comprehensive structural analysis process. However, from Table 6, the overall vulnerable location estimate results were slightly lower for the  $\{EC, UT, MW\}$  combination than for  $\{EC, UT\}$ . From Table 5, the  $\{EC, UT\}$  and  $\{EC, UT, MW\}$  combinations correctly found the same vulnerable locations in the corroded test panels, but the  $\{EC, UT\}$  combination yielded better results than the  $\{EC, UT, MW\}$  combination for finding vulnerable locations in the pristine panel for both rounds of testing. From [11], the pristine panel was slightly bent during the first round of mechanical loading, resulting in two crack locations, and a third crack was obtained during the second round of mechanical loading (see Table 2). Because there was no surface corrosion present at those crack locations, the MW modality was not able to characterize the cracks and may have skewed the fused model for pristine panel for the  $\{EC, UT, MW\}$  combination. In general, fatigue is highly sensitive to small surface features and discontinuities and is therefore statistically varied. To compound the variability, the complexity of the riveted panels used in this investigation incorporates many variables that may have affected fatigue of the panels such as residual stresses, defects, and misalignment possibly incorporated during panel assembly. Naturally, one would expect that the multi-modal fused model using the most number of modalities would produce the best results because it utilizes complementary information from the various modalities to create a more accurate picture of the corrosion environment and thus provide the best understanding of the fatigue behavior as well. In

our case, the combination of two modalities ( $\{EC, UT\}$  or  $\{EC, MW\}$ ) produced the best results as shown in Table 6 as compared to using all the three modalities. This might be attributed to the fact that the FEM based model created from nondestructive testing data is limited in its ability to predict fatigue. The inconsistency of modeling predictions is likely attributable to the dependency of model stresses on the location from which data is obtained. A predictive fatigue model would require consistently refined meshing that would allow for stress data to be obtained from the same location between modeling increments. This was not possible in our case as with each round of NDE data collection new 3-D models were generated using the testing data obtained from that particular round to be used for the FEM based fatigue analysis. Given that fatigue cracks generally nucleate in isolated locations near stress concentration sites (e.g. rivet holes), a model with refined meshing only in the fatigue sensitive regions may improve the model accuracy without significant increase to the computing power required.

Future research will explore different types of data fusion approaches to combine NDE modality data to characterize the test structures to attempt to integrate unique information from each modality. In order to address the limitations of FEM-based methods in their ability to predict fatigue, more specialized numerical modeling techniques need to be investigated which would allow the generation of a more consistently structured mesh or a consistently refined mesh in which it is possible to acquire stress data from the same location between meshing increments, which would allow for more consistent prediction of stresses.

## **VI. ACKNOWLEDGEMENT**

This work was supported in part by the Air Force Research Laboratory (AFRL) under contract no. FA8650-04-C-5704 in conjunction with the Center for Aerospace Manufacturing Technologies (CAMT).

## VII. REFERENCES

- [1] M. Brassard, A. Chahbaz, A. Pelletier, "Combined NDT inspection techniques for corrosion detection of aircraft structures," in *15th World Congress on Nondestructive Testing* Roma, Italy, 2000.
- [2] G. H. Koch, "Corrosion in Aluminum Alloy 2024-T3 Lap Joints," in *CORROSION 99*, Houston, TX, 1999.
- [3] C. L. Brooks, K. Honeycutt, S. Prost-Domasky, "Case studies for life assessments with age degradation," in *Fourth Joint DoD/FAA/NASA Conference on Aging Aircraft*, St. Louis, MO, 2000.
- [4] S. Young-Won and S. S. Udpa, "A new morphological algorithm for fusing ultrasonic and eddy current images," in *Ultrasonics Symposium, 1996. Proceedings., 1996 IEEE*, 1996, pp. 649-652 vol.1.
- [5] B. A. Lepine, B. P. Wallace, D. S. Forsyth, and A. Wyglinski, "Pulsed eddy current method developments for hidden corrosion detection in aircraft structures," *Canadian Society for Non-Destructive Testing Journal*, vol. 20, pp. 6-14, 1999.
- [6] M. A. Robers and R. Scottini, "Pulsed Eddy Current in Corrosion Detection," presented at the 8th European Conference on Nondestructive Testing, Barcelona (Spain), 2002.
- [7] J. Skramstad, R. Smith, and D. Harrison, "Enhanced detection of deep corrosion using transient eddy currents," in *7th Joint DoD/FAA/NASA Conference on Aging Aircraft*, New Orleans (USA), 2003.
- [8] D. Forsyth, J. Komorowski, "Fusion of Multimodal NDI Images for Aircraft Corrosion Detection and Quantification," in *Multi-Sensor Image Fusion and Its Applications*, ed: CRC Press, 2005, pp. 375-404.
- [9] M. T. Ghasr, S. Kharkovsky, R. Zoughi, and R. Austin, "Comparison of near-field millimeter-wave probes for detecting corrosion precursor pitting under paint," *Instrumentation and Measurement, IEEE Transactions on*, vol. 54, pp. 1497-1504, 2005.
- [10] Z. Liu, D. S. Forsyth, J. P. Komorowski, K. Hanasaki, T. Kirubarajan, "Survey: State of the Art in NDE Data Fusion Techniques," *Instrumentation and Measurement, IEEE Transactions on*, vol. 56, pp. 2435-2451, 2007.
- [11] S. De, Kapil Gupta, R. Joe Stanley, Reza Zoughi, Kenneth Doering, David Van Aken, Gary Steffes, Matt O'Keefe, and D. Palmer, "A Comprehensive Structural Analysis Process for Failure Assessment in Aircraft Lap-Joint Mimics using Intra-Modal Fusion of Eddy Current Data," *Research in Nondestructive Evaluation*, vol. 23, pp. 146-170, 2012.
- [12] N. Qaddoumi, Shroyer, A., and Zoughi, R., "Microwave Detection of Rust Under Paint and Composite Laminates " *Research in Nondestructive Evaluation* vol. 9, pp. 201-212 1997.
- [13] R. Zoughi, *Microwave Non-Destructive Testing and Evaluation*: Kluwer Academic Publishers, 2000.
- [14] M. Ghasr, B. Carroll, S. Kharkovsky, R. Zoughi, and R. Austin, "Size Evaluation of Corrosion Precursor Pitting Using Near-Field Millimeter Wave Nondestructive Testing Methods," *AIP Conference Proceedings*, vol. 760, pp. 547-553, 2005.
- [15] M.T. Ghasr, R. Zoughi, and G. Steffes, "Estimation of Corrosion Thickness under Paint using a Simple Millimeter Wave Probe," in *3rd International Conference on Electromagnetic Near-Field Characterization & Imaging (ICONIC 2007)*, St.Louis, USA, 2007, pp. 83-88.
- [16] M. T. Ghasr, D. Simms, and R. Zoughi, "Multimodal Solution for a Waveguide Radiating into Multilayered Structures - Dielectric Property and Thickness Evaluation," *Instrumentation and Measurement, IEEE Transactions on*, vol. 58, pp. 1505-1513, 2009.
- [17] J. S. Cargill, J.A. Pecina, S.M. Shepard, J.D. Weir, R. Zoughi, and A. V. Bray, "Nondestructive Testing for Corrosion Under Paint," *Materials Evaluation*, vol. 63, pp. 102-109, 2005.

- [18] V. Kaftandjian, Y. M. Zhu, O. Dupuis, D. Babot, "The combined use of the evidence theory and fuzzy logic for improving multimodal nondestructive testing systems," *Instrumentation and Measurement, IEEE Transactions on*, vol. 54, pp. 1968-1977, 2005.
- [19] X. E. Gros, L. Zheng, K. Tsukada, K. Hanasaki, "Experimenting with pixel-level NDT data fusion techniques," *Instrumentation and Measurement, IEEE Transactions on*, vol. 49, pp. 1083-1090, 2000.
- [20] B. Matuszewski, L. Shark, M. Varley, "Region-based wavelet fusion of ultrasonic, radiographic and shearography non-destructive testing images," in *15th World Conference on Nondestructive Testing*, Roma, Italy, 2000.
- [21] N. Francois, "A New Advanced Multitechnique Data Fusion Algorithm for NDT," in *15th World Congress on Nondestructive Testing* Roma, Italy, 2000.
- [22] X. E. Gros, Strachan, P., Lowden, D., and Edwards, I., "NDT data fusion," in *6th European Conference on Non-Destructive Testing*, 1994, pp. 355-360.
- [23] X. E. Gros, *NDT Data Fusion*: Halsted Press, 1996.
- [24] K. Sun, S. Udpa, L. Udpa, T. Xue, and W. Lord, "Registration issues in the fusion of eddy current and ultrasound NDE data using Q-transforms," *Review of Progress in QNDE*, vol. 15, pp. 813-820.
- [25] L. Zheng, D. S. Forsyth, J. P. Komorowski, K. Hanasaki, and T. Kirubarajan, "Survey: State of the Art in NDE Data Fusion Techniques," *Instrumentation and Measurement, IEEE Transactions on*, vol. 56, pp. 2435-2451, 2007.
- [26] T. Doppke and A. Bryant., "The Salt Spray Test: Past, Present, and Future," in *2nd Automotive Corrosion Prevention Conference*, 1983, pp. 57-72
- [27] K. Gupta, R. J. Stanley, M. T. Ghasr, S. Kharkovsky, R. Zoughi, G. Steffes, "Fusion of Multimodal NDE Data for Improved Corrosion Detection," in *3rd International Conference on Electromagnetic Near-Field Characterization and Imaging*, St.Louis, MO, 2007, pp. 407-412.
- [28] K. Gupta, M. T. Ghasr, S. Kharkovsky, R. Zoughi, R. J. Stanley, A. Padwal, M. O'Keefe, D. Palmer, J. Blackshire, G. Steffes, and N. Wood, "Fusion of Microwave and Eddy Current Data for a Multi-Modal Approach in Evaluating Corrosion Under Paint and in Lap Joints," *AIP Conference Proceedings*, vol. 894, pp. 611-618, 2007.
- [29] S. De, K. Gupta, R. J. Stanley, G. Steffes, D. Palmer, R. Zoughi, "A data fusion based approach for evaluation of material loss in corroded aluminum panels," in *ITSC '09. 12th International IEEE Conference on Intelligent Transportation Systems*, St. Louis, MO, 2009, pp. 1-6.
- [30] J. K. Hackett, M. Shah, "Multi-sensor fusion: a perspective," in *Robotics and Automation, 1990. Proceedings., 1990 IEEE International Conference on*, 1990, pp. 1324-1330 vol.2.
- [31] D. Hughes, Wang, N., Case, T., Donnell, K., Zoughi, R., Austin, R. and Novack, M., "Microwave nondestructive detection of corrosion under thin paint and primer in aluminum panels," *Special Issue of Subsurface Sensing Technologies and Applications: on Advances and Applications in Microwave and Millimeter Wave Nondestructive Evaluation* vol. 2, pp. 435-451, 2001.